

Converting the sub-Jovian desert of exoplanets to a savanna with TESS, PLATO and Ariel

Szilárd Kálmán,^{1,2,3,4,5}★ Gyula M. Szabó,^{2,6,7} Luca Borsato,⁸ Attila Bódi,^{1,5,10} András Pál^{1,5} and Róbert Szabó^{1,5,9,10}

¹Konkoly Observatory, Research Centre for Astronomy and Earth Sciences, ELKH, MTA CSFK Lendület Near-Field Cosmology Research Group, Konkoly-Thege Miklós út 15–17., H-1121, Hungary

²MTA-ELTE Exoplanet Research Group, Szombathely, Szent Imre h. u. 112., H-9700, Hungary

³ELTE Eötvös Loránd University, Doctoral School of Physics, Budapest, Pázmány Péter sétány 1/A, H-1117, Hungary

⁴Graduate School of Physics, University of Szeged, Szeged, Dóm tér 9., H-6720, Hungary

⁵CSFK, MTA Centre of Excellence, Budapest, Konkoly Thege Miklós út 15-17., H-1121, Hungary

⁶ELTE Eötvös Loránd University, Gothard Astrophysical Observatory, Szombathely, Szent Imre h. u. 112., H-9700, Hungary

⁷MTA-ELTE Lendület "Momentum" Milky Way Research Group, Hungary

⁸INAF-Osservatorio Astronomico di Padova a Vicolo dell'Osservatorio 5, 35122, Padova, Italy

⁹Eötvös Loránd University, Institute of Physics, Pázmány Péter sétány 1/A, H-1171 Budapest, Hungary ¹⁰MTA CSFK Lendület Near-Field Cosmology Research Group

Accepted XXX. Received YYY; in original form ZZZ

ABSTRACT

There is a lack of exoplanets with sizes similar to Neptune orbiting their host stars with periods $\lesssim 3$ days – hence the name “sub-Jovian/Neptune desert”. Recently, several exoplanets have been confirmed to reside in the desert transforming it into a “savanna” with several “giraffe” planets (such as LTT 9779 b and TOI-674 b). The most prominent scenarios put forward for the explanation of the formation of the desert are related to the stellar irradiation destroying the primary atmosphere of certain specific exoplanets. We aim to present three targets (LTT 9779 b, TOI-674 b and WASP-156 b) which, when observed at wide wavelength ranges in infrared (IR), could prove the presence of these processes, and therefore improve the theories of planetary formation/evolution. We simulate and analyse realistic light curves of the selected exoplanets with PLATO/NCAM and the three narrow-band filters of Ariel (VISPhot, FGS1 and FGS2) based on TESS observations of these targets. We improved the precision of the transit parameters of the three considered planets from the TESS data. We find that the combination of the three narrow-band filters of Ariel can yield inner precision of $\lesssim 1.1\%$ for the planetary radii. Data from the three telescopes together will span decades, allowing the monitoring of changes in the planetary atmosphere through radius measurements. The three selected “giraffe” planets can be golden targets for Ariel, whereby the loss of planetary mass due to stellar irradiation could be studied with high precision, multi-wavelength (spectro-)photometry.

Key words: exoplanets – methods: observational – techniques: photometric

1 INTRODUCTION

An enigmatic “hole” in the exoplanet distribution, the lack of exoplanets ranging between Jupiters and super-Earths in size and with orbital periods $\lesssim 3$ days was reported by Szabó & Kiss (2011) and was later confirmed by Mazeh et al. (2016). This region in the mass–period ($M_P - P$) and radius–period ($R_P - P$) parameter spaces was named the sub-Jovian/Neptune desert of exoplanets. The presence of an ever-increasing number of objects in the sub-Jovian desert such as NGTS-4b (West et al. 2019), NGTS-5b (Eigmüller et al. 2019), LTT 9779b Jenkins et al. (2020), TOI-849b (Armstrong et al. 2020), TOI-674b (Murgas et al. 2021), NGTS-14Ab (Smith

et al. 2021), or TOI-2196b (Persson et al. 2022) suggests that it is not completely empty. With the increasing number of confirmed exoplanets, it is reasonable to expect that the number of known exoplanets will increase in the future. Because TOI-674 b resides inside the sub-Jovian desert, Murgas et al. (2021) introduced the term “oasis” for it. The detection of water vapor in its atmosphere (Brande et al. 2022) could also be in line with this terminology. However, without the confirmation that all planets in this area of the parameter spaces have a water-rich atmosphere, we suggest the term “sub-Jovian savanna” for the area in question (see Szabó et al. (2023) for details), while calling the individual planets “giraffes” in the savanna. The naming of the objects is justified as these planets were the first (i.e. the easiest) to be discovered in the savanna, sim-

★ E-mail: xilard1@gothard.hu

ilarly to their namesake animals, which can easily be seen from a long distance.

There are a number of proposed explanations for the savanna (see Owen & Lai (2018) and Szabó et al. (2023) for an overview), however, photoevaporation of close-in exoplanets seems to play an essential role in its formation (Owen & Lai (2018); Szabó & Kálmán (2019)). In Szabó et al. (2023), we explored the dependencies of the savanna across the HRD parameters in search of correlations and implications on how these regions of the period-mass and period-radius parameter spaces are formed, confirming the role of photoevaporation while also pointing out that it alone cannot explain this phenomenon. In this paper, we focus on the observational aspects of the understanding of the savanna. For this purpose, we selected three known exoplanets, LTT 9779 b, and WASP-156 b (Demangeon et al. 2018a) which are in the savanna.

The TESS (Ricker et al. 2015) light curve from S2 of LTT 9779 b was analyzed by Jenkins et al. (2020). Crossfield et al. (2020) and Dragomir et al. (2020) have explored its bulk composition and atmosphere based on Spitzer IRAC (Fazio et al. 2004) observations. Ground-based transit observations from the Las Cumbres Observatory and the Next Generation Transit Survey (Wheatley et al. 2018) were also included in the analysis that confirmed the planetary nature of LTT 9779 b. The planetary nature of the companion of the nearby M dwarf TOI-674 was confirmed by Murgas et al. (2021) with the help of ground-based and Spitzer observations. Both Murgas et al. (2021) and Brande et al. (2022) reported that the super-Neptune is present in the Neptune desert. In their analysis, Brande et al. (2022) analyzed the TESS light curves from S9, S10 and S36, while also incorporating data obtained by the Hubble Space Telescope with a focus on the planetary atmosphere. The super-Neptune WASP-156 b was discovered by Demangeon et al. (2018a). Saha & Sengupta (2021) analyzed the TESS light curves from S4 and S31 via wavelet denoising and GP regression techniques. The transit parameters were also derived by Yang et al. (2022) based on TESS observations and the Gaia database (Gaia Collaboration et al. 2016, 2018).

In this paper, we aim to demonstrate how direct observational evidence can be gained by observing the giraffe exoplanets for testing the atmospheric mass-loss-based scenarios (Szabó et al. 2023) for the evolution of the savanna via observations with PLATO (Rauer et al. 2014, Planetary Transits and Oscillations of stars) and Ariel (Atmospheric remote-sensing infrared exoplanet large survey; Tinetti et al. 2021). We propose that by constraining the transit depth through optical and near-infrared (NIR) measurements, the wavelength-dependence of the transit depth, expected in IR, can be attributed to the loss of an extended atmosphere of the giraffes. Such observations will be possible with Ariel.

This paper is structured as follows. In Sec. 2, we discuss the TESS observations of the three selected planets, present our methods for the derivation of the transit parameters, and show the simulated light curves of Ariel and PLATO. In Sec. 3, the improved transit parameters based on the TESS light curves are presented, while we show the results from the simulated light curves in Sec. 4. Finally, we discuss the time- and wavelength-dependence of R_p and the observational prospects presented by the upcoming ESA missions (Sec. 5).

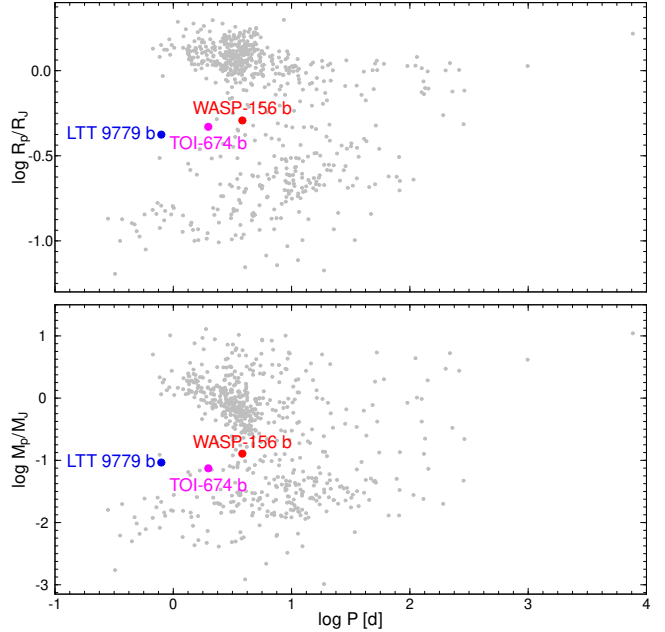


Figure 1. Position of the three selected planets in the radius-period and mass-period planes. LTT 9779 b and TOI-674 b clearly populate the sub-Jovian savanna in both cases, while WASP-156 b is on the border. The planetary parameter database is the same as in Szabó et al. (2023).

2 METHODS

In this section, we describe the light curve solutions for the available TESS data, as well as the simulations for the Ariel and PLATO missions.

2.1 Target selection: populating the desert

From the sample of all known exoplanets in the NASA Exoplanet Archive¹, we selected three planets (LTT 9779 b, TOI-674 b and WASP-156 b, Fig. 1) the detailed analysis of which can lead to obtaining observational evidence of how the savanna is formed. We selected LTT 9779 as it clearly resides in the savanna in both $M_p - P$ and $R_p - P$ parameter planes (Fig. 1). Given that there is a small number of known planets in these regions of the parameter planes, the other two objects so that they are on the boundaries: TOI-674 b is “inside” only in the $R_p - P$ plane (upper panel of Fig. 1), while WASP-156 b is on the border in both parameter spaces. A further criteria for the selection was the availability of TESS observations. We focus on the information that can be gained from the best currently available optical light curves and show the validity of future observations with the next generation of space-based observatories.

2.2 Observations with TESS

All three systems were observed by TESS in at least two sectors: S2 and S29 for LTT 9779; S9, S10 and S36 for TOI-674; S3, S31, S42 and S43 for WASP-156. We used the `lightkurve` software package (Lightkurve Collaboration et al. 2018) to obtain the 2-min

¹ <https://exoplanetarchive.ipac.caltech.edu/>

cadence Simple Aperture Photometry (SAP) light curves of all three targets. We removed all measurements with non-zero quality flags and combined the data from all sectors of each star, which resulted in light curves of 34232, 46427 and 58041 data points for LTT 9779, TOI-674 and WASP-156, respectively. In the case of LTT 9779, we also removed data containing the first transit because of severe baseline variations. We also removed several artefacts from the SAP flux light curve of WASP-156 around 2490 BTJD.

2.3 Light curve solutions

We made use of the Transit and Light Curve Modeller (TLCM; Csizmadia 2020) code to analyze the light curves. This software incorporates the analytic Mandel-Agol transit model (Mandel & Agol 2002) with four parameters: the scaled semi-major axis, a/R_S , the ratio of the planetary and stellar radii, R_P/R_S , the impact parameter, $b = a/R_S \cos i$ (where i is the orbital inclination relative to the line of sight) and the time of midtransit, t_C . These parameters, as well as the orbital period P , were left free in all three cases. We made use of PyLDtk (Parviainen & Aigrain 2015) to compute the quadratic limb-darkening coefficients u_1 and u_2 . The PHOENIX-generated stellar spectra used for these calculations (Husser et al. 2013) were selected based on T_{eff} , $\log g$ and $[\text{Fe}/\text{H}]$ (Table 3). During the fitting process, TLCM uses $u_+ = u_1 + u_2$ and $u_- = u_1 - u_2$.

TLCM also relies on the wavelet-formulation of Carter & Winn (2009) to handle time-correlated noise, which arises as the combination of stellar variability and instrumental effects. In this approach, the noise is described by two parameters: σ_r for the red component and σ_w for the white component. The fitting process is then done for the noise plus transit model simultaneously. The wavelet-based noise handling approach of TLCM has a regularization condition to avoid overfitting the noise: the standard deviation of the residuals are decreased until they are equal to the average photometric uncertainty of the input light curve (Csizmadia et al. 2021). While σ_w is representative of the amount of white noise present in the light curves, σ_r is not related to the root mean squared of the red noise (Carter & Winn 2009; Csizmadia et al. 2021). The usage of the wavelet-formulation was tested on noise sources with timescales ranging from several tens of seconds (Kálmán et al. 2022a) to tens of minutes (Kálmán et al. 2022b) to several hours or days (Csizmadia et al. 2021), and it was found to yield consistent results in every case. We assumed circular orbits for all three planets and the adopted stellar parameters are shown in Table 3.

2.4 Simulated Ariel observations

Our simulations were focused on the three narrow band filters that will be available for Ariel observations (Tinetti et al. 2021; Szabó et al. 2022a): VISPhot, FGS1 and FGS2. At the time of writing, there was no available simulator dedicated for Ariel observations. Neglecting out-of-transit variations, the observed light curves of exoplanet-hosting stars consist of three parts: transit signal; white noise and red noise. The white component was assumed to be made up of four sources (Mugnai et al. 2020): (i) Poisson noise term, (ii) detector noise term, (iii) jitter noise term and (iv) the Payload noise floor. The noise budget for this component was calculated by ArielRad (Mugnai et al. 2020) and it is different at the three used wavelengths. The time-correlated noise (see e.g. Figs. 3, 5 and 7) can arise from several sources, including instrumental effects and astrophysical phenomena (including flares, granulation, pulsation, etc.) and is therefore dependent on both stellar and instrumental

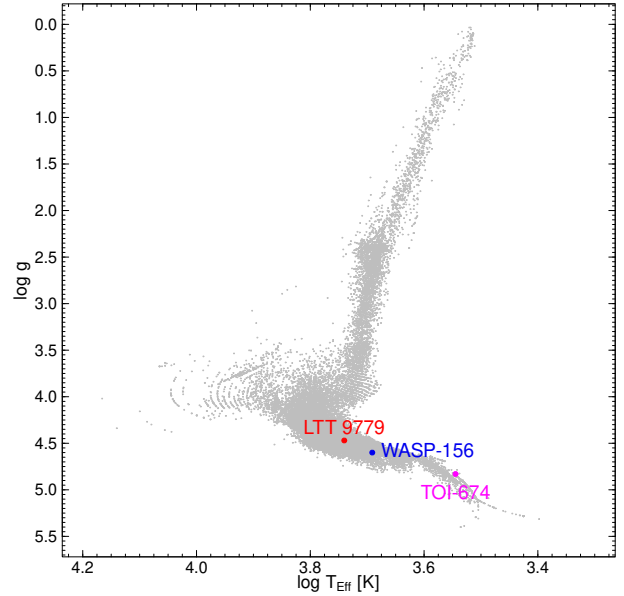


Figure 2. Kiel diagram showing the stars from Huber et al. (2014). The position of the three host stars was used for selecting relevant Kepler light curves for the simulated Ariel observations (see text for details).

parameters. The exact nature of correlated noise expected from the Ariel detectors is not known. We therefore proceeded to use Kepler observations of similar stars to those which host the three giraffe planets. These targets were identified from the database of Huber et al. (2014) based on the stellar parameters from Table 3, the position of LTT 9779, TOI-674 and WASP-156 on the Kiel diagram from this database is shown in Fig. 2. After downloading two adjacent Quarters of long cadence SAP flux light curves for each target via the `lightkurve` software package, we detrended and fitted an Autoregressive Integrated Moving Average (ARIMA) model to each of them. The noise levels for the two noise types (white and red) of the three stars observed by Kepler are listed in Table 1. These quantities are calculated as the standard deviation of the residuals of the ARIMA processes and the fitted ARIMA processes themselves in a one-hour bin. Note that during the selection of the Kepler targets, we did not take brightness into account, resulting in higher white noise levels in comparison with Ariel.

The color-dependence of the correlated noise is not well understood. Based on prior experience, it is clear that the amplitude of the red noise decreases with longer wavelength, but no exact relationship has been established yet. Because Ariel will be able to perform simultaneous observations with different filters, it will also provide opportunities to handle this question. We simulated three separate ARIMA models with the Kepler cadence for all three stars. Then we normalized the standard deviations of these red noise models. Finally, we scaled the noise levels in the three filters by heuristically assuming that noise amplitude in VISPhot will be the same as in the Kepler observations, while in FGS1 and FGS2, the amplitude was set to $0.95\times$ and $0.90\times$ the Kepler-levels. We then proceeded to interpolate the 1800 s cadence noise models to 1 s, the lowest nominal exposure time of Ariel. The red noise levels listed in Table 1 are calculated as the standard deviation of these time series, binned to one hour intervals. Note that the time-correlated noise can not be interpreted as Gaussian, therefore, the variance of the binned data

does not scale with the length of the bins. This is the reason behind the apparent discrepancy between the Kepler and Ariel noise levels seen in Table 1. Finally, we added a Gaussian noise model with standard deviation derived from the noise budget of ArielRad, yielding a conservative total noise estimate. The white noise levels, computed as the standard deviation of the data binned to one-hour intervals, are also listed in Table 1.

For the synthetic transits, we made use of the `batman` software package (Kreidberg 2015), which incorporates a Mandel-Agol model. Using PyLDTk, based on the stellar parameters of Table 3, we calculated the four parameter limb-darkening coefficients (Claret 2000) for all three stars (Table 2), and created the synthetic transit light curves from our derived transit parameters of Tables 4, 5 and 6 at the 1 s cadence.

After injecting the transits (with fixed P and t_C) into the noise model, we binned the light curves to 60 seconds for LTT 9779 b and TOI-674 b and to 30 seconds for WASP-156 b to mimic the real observations that will be made with Ariel. This also allowed us to have a realistic estimate of the photometric uncertainties, which are used by TLCM to constrain the correlated noise (see Csizmadia et al. (2021) for more details).

We note that the observing strategy of Ariel will be completely different than in the case of Kepler, therefore, the systematic noise sources can be expected to differ significantly as well. So far, however, no specific instrumental noise models exist for Ariel. Therefore, our assumption of a Kepler-like red noise profile that is scaled according to wavelength is not perfectly representative of the so far unknown Ariel systematics, however, it is still considerably more realistic than assuming white noise alone.

2.5 Simulated PLATO observations

PLATO Solar-like Light-curve Simulator (PSLS; Samadi et al. 2019) is a tool for generating realistic light curves representative of the performance of the PLATO mission. PSLS is designed to perform hare-and-hound exercises to characterize the expected performance of the multi-camera concept. This tool can simultaneously simulate solar-like oscillations, stellar granulation, and magnetic activity along with random noise and systematic errors. The latter two is based on pixel level simulations and contain the effect of periodic mask updates, introducing jumps in the light curves.

In this paper, we used the publicly available PSLS² (v1.4) python software. To simulate light curves we only considered instrumental noise and systematic effects. It is important to note that contrary to the simulated Ariel observations, all sources of stellar noise have been omitted. We simulated 90 days long observation sequences, where the random noise was taken from tables generated from realistic light curves. We considered two cases: in the most favorable case, the giraffes may be observed by all four camera groups (each consisting of six cameras), while in the less favorable case, they may be observed with only one group (see e.g. Nascimbeni et al. (2022) and Heller et al. (2022) for details). When the ideal circumstances are present (i.e. observations with all 24 so-called normal cameras are feasible, we averaged the data of all four camera groups with all six cameras each to obtain the final light curves, while in the other case we used the PSLS data for one group. For long-term stellar drift, we simulated the worst-case scenario, setting the drift level to its maximum value. The input stellar magnitudes and effective temperatures were set according to the given target's

values. All the other PSLS parameters were kept at their default values.

To account for the possible stellar activity, we also included the noise models from the Kepler observations as described in Sect. 2.4. This way, we also introduce further systematic effects that were characteristic of the Kepler observations, however, we get more conservative estimates for the retrieved parameters. The added red noise was scaled as in the case of VISPhot. The noise levels, calculated as in Sect. 2.4, are also listed in Table 1 for the two considered cases: observations with 6 and 24 cameras. We then injected the planetary signals in the same way as for the Ariel simulations: the light curves were created with the `batman` software with transit parameters derived from the TESS light curves, while using the 4-parameter limb-darkening coefficients from Table 2. PLATO limb-darkening coefficients were calculated using ExoTETHyS (Morello et al. 2020b,a). We employed state-of-the-art spectral response of the PLATO instruments, the MARCS stellar atmosphere grid (Gustafsson et al. 2008) and Non-LTE Turbospectrum models (Gerber et al. 2022) computed within the PLATO consortium. The photometric uncertainty was set to the standard deviation of the noise model. We used the nominal cadence of 25 s (with 21 s exposure times).

It is important to point out that we used TLCM to solve the light curves in every case, which also yielded consistent uncertainty estimations, which enabled straight-forward comparisons of the transit parameters between the different telescopes/instruments. We chose 30-day-long simulated light curves for both the Ariel and PLATO analyses, because a time series of this length contains roughly the same number of transits as a single Sector of TESS.

3 TRANSIT PARAMETERS FROM TESS

Following the recipe of Sec. 2, we made use of TLCM to derive transit parameters from the TESS light curves, which were subsequently used in the Ariel and PLATO simulations.

3.1 LTT 9779 b

Our analysis of LTT 9779 b is based on two sectors of SAP flux data (Fig. 3, top panel). We adopted the following stellar parameters for the host from Jenkins et al. (2020): $T_{eff} = 5499 \pm 50$ K, $\log g = 4.47 \pm 0.10$, $[Fe/H] = 0.31 \pm 0.08$ and $R_S = 0.92 \pm 0.01 R_\odot$ (Table 3). In the cases of the light curves of the giraffes, the S/N was not high enough to fit the limb-darkening parameters, even when applying Gaussian priors to them, so we opted to fix them at their theoretical values as calculated by PyLDTk ($u_{+,TESS} = 0.62$ and $u_{-,TESS} = 0.39$ for LTT 9779).

The best-fit transit model is shown on the upper panel of Fig. 3 (as a function of time) and Fig. 4 (as a function of orbital phase). The residuals of the best-fit models (lower panels of Figs. 3 and 4) indicate that much of the correlated noise (middle panel of 3) was removed as a consequence of the wavelet-based noise handling. The fitted transit parameters are shown in Table 4. These parameters are in excellent agreement with the results of Jenkins et al. (2020) (except for the noise terms of TLCM). Our analysis also improved the precision of the transit parameters which is the result of the correlated noise treatment of TLCM and basically double the available photometric data. The greatest improvements are observable at the orbital period with $P = 0.79206447 \pm 2.9 \cdot 10^{-7}$ days (an uncertainty of 0.025 seconds) and the ratio of the planetary and stellar radii with $R_P/R_S = 0.04578 \pm 0.00066$. The latter translates to

² <https://sites.lesia.obspm.fr/psls/>

Table 1. White and red noise levels used in the simulations for the three targets in the three Ariel pass-bands (VISPhot, FGS1 and FGS2), the two considered cases for the PLATO visits (6 and 24-camera observations) and the noise levels for the Kepler data, expressed as point-to-point scatter in one-hour bins. These values are calculated as the standard deviation of each noise model (see text for more details). Note that the Kepler noise levels are calculated for the stars which were chosen as the source for the red noise.

Parameter	LTT 9779					TOI-674					WASP-156							
	VISphot	FGS1	FGS2	PLATO 24	PLATO 6	Kepler	VISphot	FGS1	FGS2	PLATO 24	PLATO 6	Kepler	VISphot	FGS1	FGS2	PLATO 24	PLATO6	Kepler
WN [ppm \sqrt{h}]	66	50	47	26	49	286	354	132	78	230	434	310	145	83	71	61	126	286
RN [ppm \sqrt{h}]	126	121	116		85	213	120	112	102		122	208	143	136	127	134		265

Table 2. Limb-darkening coefficients of the three host stars for PLATO and the three narrow-band filters of Ariel.

Host name	Instrument	4-parameter law				Quadratic law	
		u_1	u_2	u_3	u_4	u_1	u_2
LTT 9779	Ariel/VISPhot	0.084	0.101	1.074	-0.518	0.725	0.059
	Ariel/FGS1	-0.128	1.031	-0.227	-0.041	0.544	0.110
	Aiel/FGS2	-0.139	1.133	-0.555	0.090	0.410	0.120
	PLATO/NCAM	0.632	-0.345	0.807	-0.325	0.517	0.134
TOI-674	Ariel/VISPhot	-0.142	2.015	-1.501	0.438	0.552	0.231
	Ariel/FGS1	0.065	1.634	-1.459	0.461	0.380	0.245
	Aiel/FGS2	0.687	-0.128	0.133	-0.084	0.235	0.210
	PLATO/NCAM	0.729	0.298	-0.226	0.061	0.389	0.291
WASP-156	Ariel/VISPhot	0.063	0.524	0.356	-0.167	0.754	0.021
	Ariel/FGS1	0.031	0.842	-0.194	0.001	0.565	0.099
	Aiel/FGS2	0.033	0.888	-0.439	0.092	0.424	0.115
	PLATO/NCAM	0.566	-0.311	0.865	-0.341	0.580	0.099

Table 3. Stellar parameters used in the light curve analysis. Adopted from Jenkins et al. (2020) (LTT 9779), Murgas et al. (2021) (TOI-674) and Demangeon et al. (2018a) (WASP-156).

Parameter	LTT 9779	TOI-674	WASP-156
T_{eff} [K]	5499 ± 50	3505 ± 30	4910 ± 61
$\log g$	4.47 ± 0.10	4.83 ± 0.01	4.60 ± 0.05
$[Fe/H]$	0.31 ± 0.08	0.114 ± 0.074	0.24 ± 0.12
R_S/R_{\odot}	0.92 ± 0.01	0.42 ± 0.01	0.76 ± 0.04
V [mag]	9.76	14.203	11.59

an absolute radius of $R_P = 0.419 \pm 0.061 R_J$, locating the planet firmly in the sub-Jovian savanna, and qualifying it as a giraffe.

The white noise parameter, σ_w , roughly corresponding to the standard deviation of the residuals, implies 90 ppm \sqrt{h} noise level in a one-hour bin, which is almost double of the noise level expected in FGS2 (Table 1).

3.2 TOI-674 b

Following Brande et al. (2022), we re-analyzed the three sectors of TESS data with TLMC of TOI-674 b. We adopted the stellar parameters from Murgas et al. (2021) (Table 3) and computed the following limb-darkening coefficients with PyLDTK: $u_{+, \text{TESS}} = 0.59$ and $u_{-, \text{TESS}} = 0.07$. The complete filtered SAP flux light curve is shown on the upper panel of Fig. 5. The identified red noise is plotted on the middle panel of Fig. 5; the noise corrected observed light curve; the best fit transit model and the residuals are shown on the upper and lower panels of Figs. 5 and 6 (as a function of time and orbital phase, respectively).

Our best-fit transit parameters for TOI-674 b (Table 5) are $\sim 1\sigma$

Table 4. Comparison of our derived transit parameters for LTT 9779b to the results of Jenkins et al. (2020). The time of midtransit is expressed in BJD - 2457000.

Parameter	This work	Jenkins et al. (2020)
a/R_S	3.777 ± 0.053	$3.877^{+0.090}_{-0.091}$
R_P/R_S	0.04578 ± 0.00066	$0.0455^{+0.0022}_{-0.0017}$
b	0.9241 ± 0.0025	$0.912^{+0.050}_{-0.049}$
P [days]	$0.79206447 \pm 2.9 \cdot 10^{-7}$	$0.7920520 \pm 9.3 \cdot 10^{-7}$
t_C [TBJD]	1355.00699 ± 0.00018	1354.21430 ± 0.00025
σ_r [100 ppm]	248 ± 8	–
σ_w [100 ppm]	4.956 ± 0.025	–

from the results of Murgas et al. (2021) for a/R_S , b , t_C and P . In the case of the star-to-planet radius ratio, our results are 2.62σ lower than the previously published values, this is statistically still negligible. The fact that Murgas et al. (2021) find slightly deeper transits for TOI-674 b may be attributed to the fact that we do not include ground-based data and that we use theoretical limb-darkening coefficients.

Based on the wavelets, the white noise present in the TESS light curve is 438 ppm \sqrt{h} .

3.3 WASP-156 b

Our analysis of WASP-156 b was based on the combined SAP flux light curves from S4, S31, S42 and S43 (Fig. 7, top panel). We adopted the stellar parameters from Demangeon et al. (2018a) (Table 3) using which the following limb-darkening coefficients

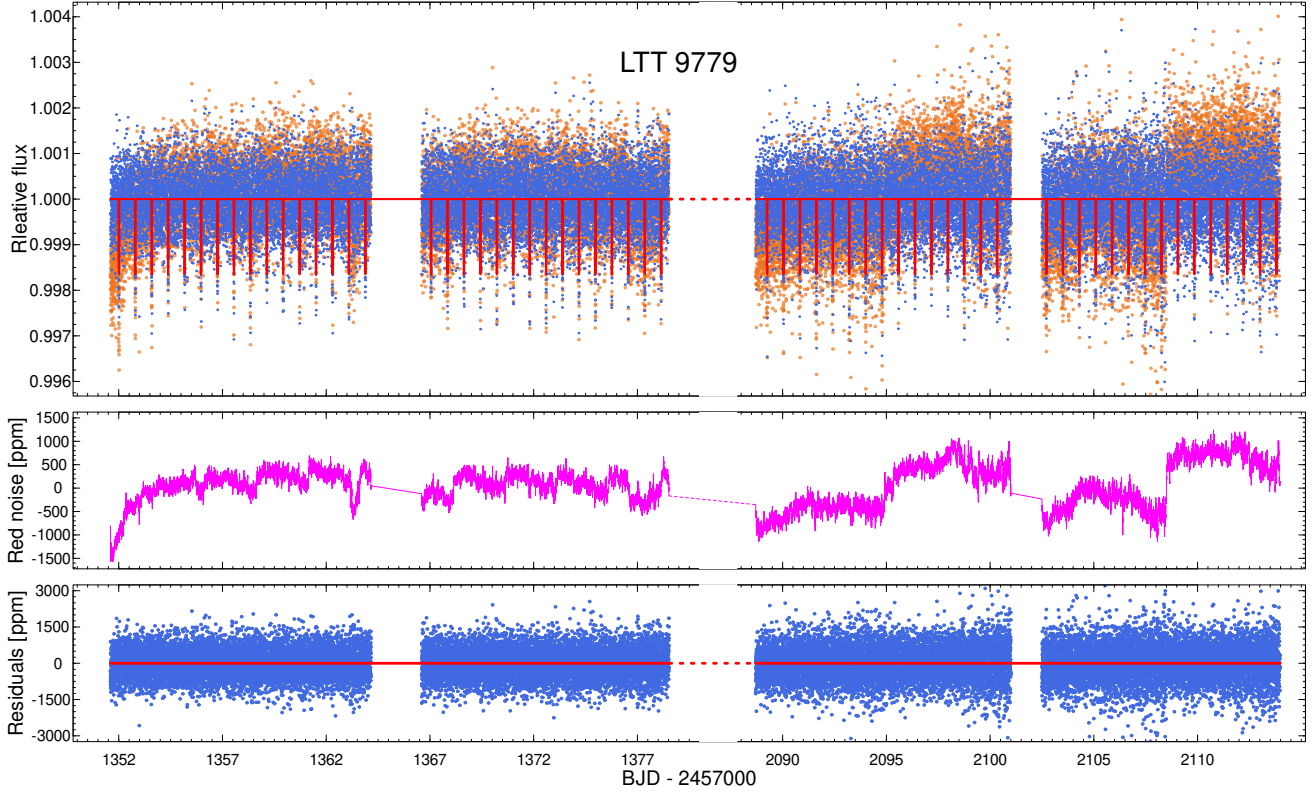


Figure 3. Observed TESS light curve of LTT 9779 from Sectors 2 and 29 (top panel, orange dots) – note the break on the time axis. Subtracting the fitted red noise (middle panel) from the observations yields the blue dots of the top panel. The best fit transit model is shown with continuous red line. The residuals are plotted on the bottom panel.

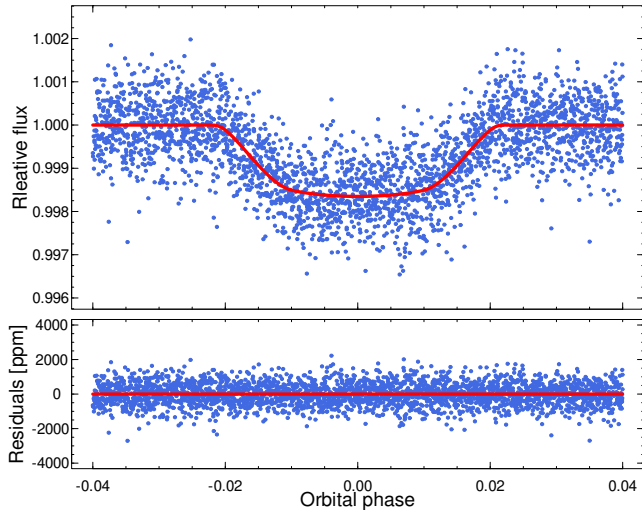


Figure 4. Phase-folded TESS light curve of LTT 9779 without correlated noise (top panel, blue dots), the best fit transit model (top panel, solid red line) and the residuals (bottom panel).

were computed by PyLDTK: $u_{+,TESS} = 0.62$, $u_{-,TESS} = 0.42$. The best-fit transit model is shown on the upper panels of Figs. 7 and 8; the residuals (after the removal of the red noise, shown on the

Table 5. Comparison of our derived transit parameters for TOI-674b to the results of Murgas et al. (2021).

Parameter	This work	Murgas et al. (2021)
a/R_S	12.15 ± 0.26	12.80 ± 0.42
R_P/R_S	0.11163 ± 0.00095	0.1140 ± 0.0009
b	0.666 ± 0.017	0.624 ± 0.035
P [days]	$1.97716410 \pm 8.4 \cdot 10^{-7}$	$1.977143 \pm 30 \cdot 10^{-7}$
t_C [TBJD]	1544.52421 ± 0.00017	1641.40455 ± 0.00010
σ_r [100 ppm]	1003 ± 25	–
σ_w [100 ppm]	24.083 ± 0.101	–

middle panel of Fig. 7) are plotted on the lower panels of Figs. 7 and 8.

The fitted transit parameters are shown in Table 6. All of these are in good agreement with the previous results of Demangeon et al. (2018a); Saha & Sengupta (2021) Yang et al. (2022). Although our determined uncertainties are considerably larger than the ones given by Saha & Sengupta (2021), Kálmán et al. (2022a) showed that the TLMC approach of error estimation yields consistent results.

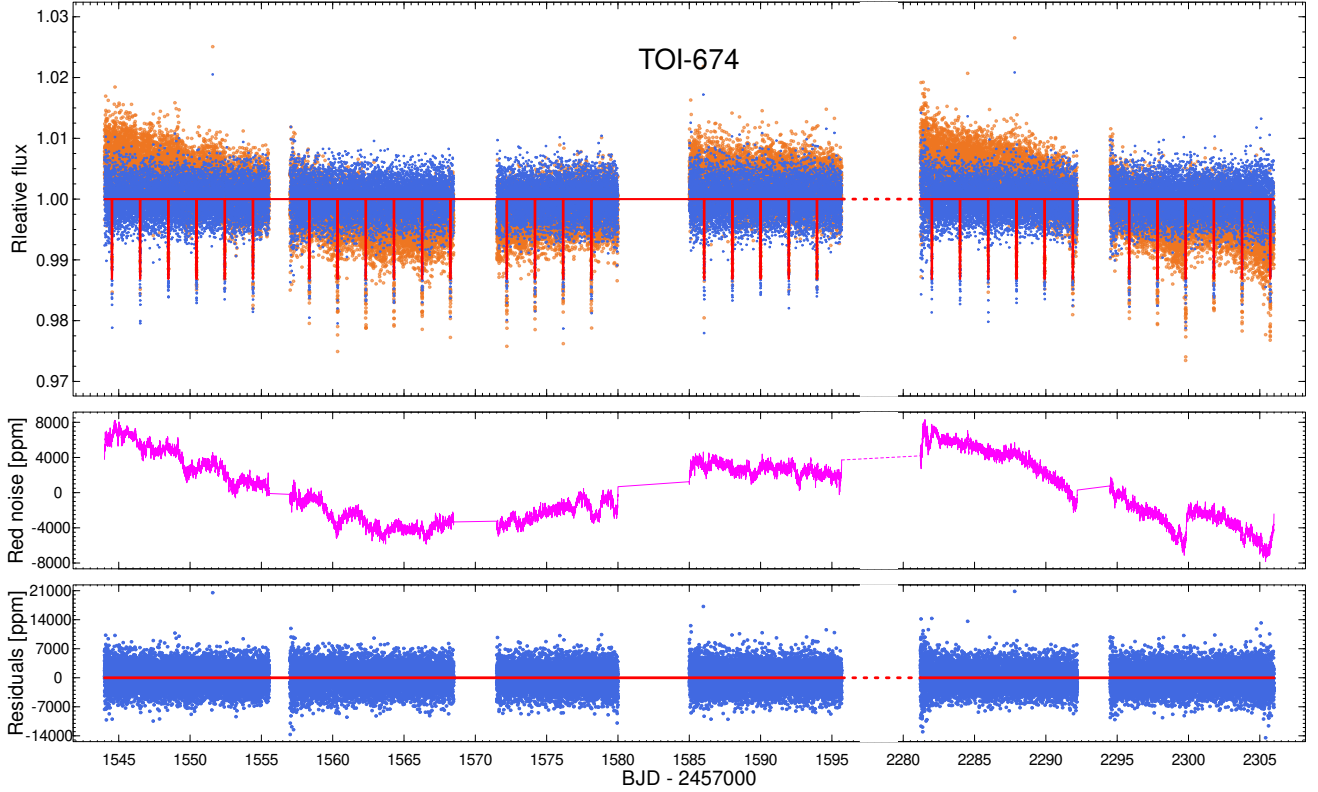


Figure 5. Observed TESS light curve of TOI-674 from Sectors 9, 10, and 36 (top panel, orange dots) – note the break on the time axis. Subtracting the fitted red noise (middle panel) from the observations yields the blue dots of the top panel. The best fit transit model is shown with continuous red line. The residuals are plotted on the bottom panel.

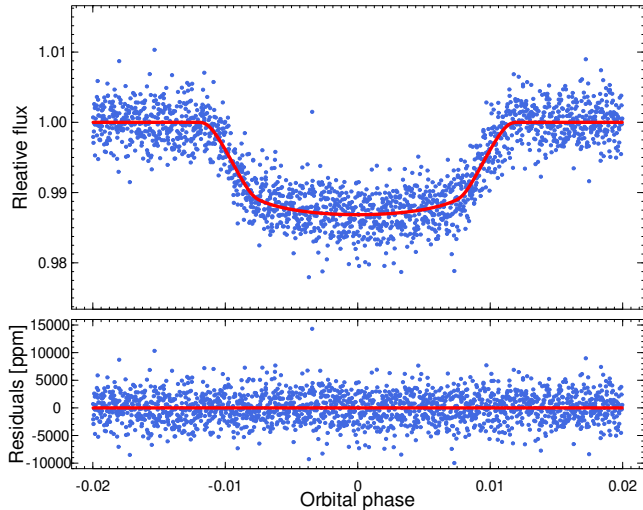


Figure 6. Phase-folded TESS light curve of TOI-674 without correlated noise (top panel, blue dots), the best fit transit model (top panel, solid red line) and the residuals (bottom panel).

4 PROSPECTS WITH ARIEL AND PLATO: OBSERVING THE GIRAFFES

An even better understanding of how the sub-Jovian savanna is formed can be achieved, from an observational point of view, in

Table 6. Comparison of our derived transit parameters for WASP-156 to the results of Saha & Sengupta (2021).

Parameter	This work	Saha & Sengupta (2021)
a/R_S	12.83 ± 0.33	$12.748^{+0.025}_{-0.027}$
R_P/R_S	0.06625 ± 0.00087	$0.067654^{+0.000082}_{-0.000060}$
b	0.18 ± 0.13	$0.2445^{+0.0061}_{-0.0073}$
P [days]	$3.8361604 \pm 2.1 \cdot 10^{-6}$	$3.8361603 \pm 4.8 \cdot 10^{-7}$
t_C [TBJD]	1414.13598 ± 0.00046	1414.136153 ± 0.000065
σ_r [100 ppm]	640 ± 17	
σ_w [100 ppm]	14.490 ± 0.078	

two ways: precise determination of planetary parameters for many exoplanets (by e.g. the PLATO mission) or bespoke observations for several candidates (by e.g. the James Webb Space Telescope or Ariel). We performed simulated observations with PLATO and Ariel for the three giraffes described in Sec. 2 to see how we can improve our understanding of the savanna by refining the transit parameters with these two upcoming ESA missions.

4.1 Transit parameters from Ariel

We fitted the simulated Ariel light curves in the three filters (VIS-Phot, FGS1 and FGS2) independently of one another for all three targets. The phase-folded input light curves and the best-fit models

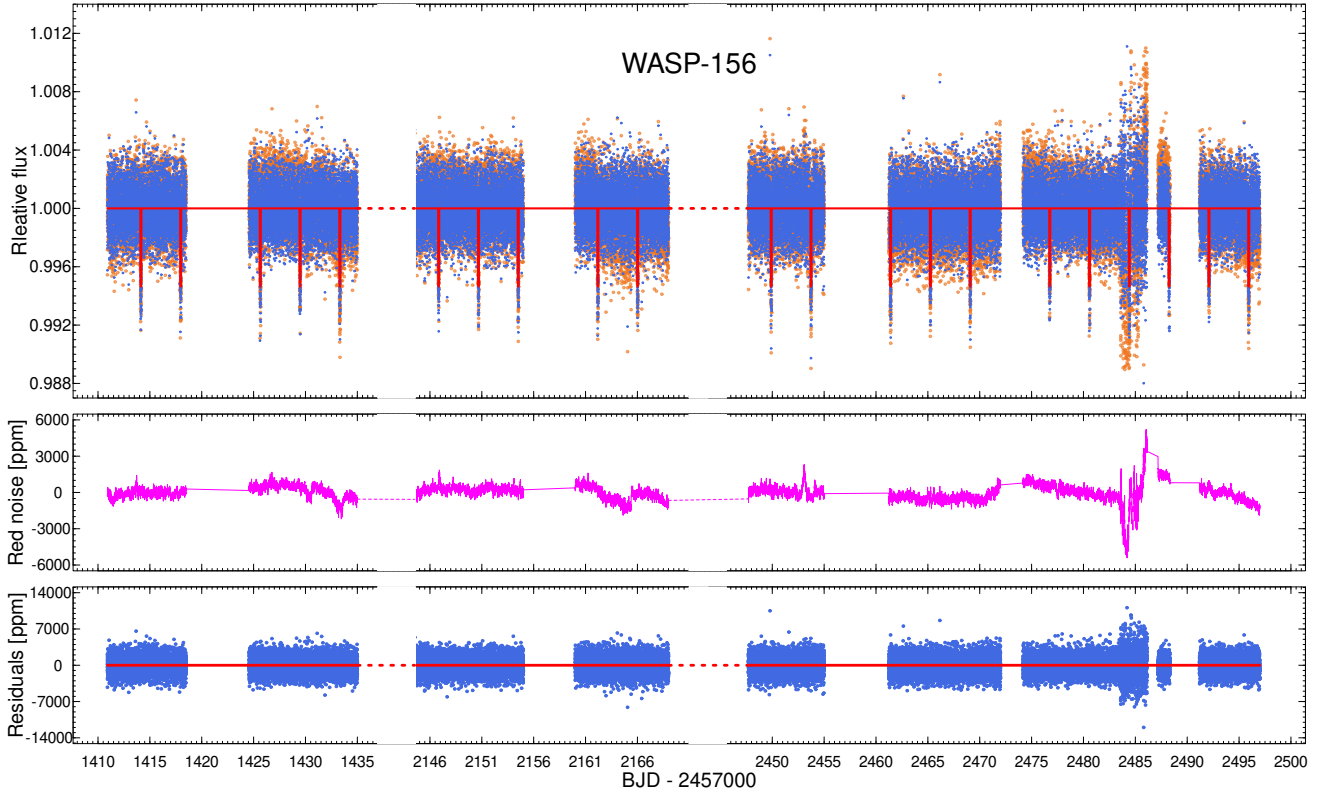


Figure 7. Observed TESS light curve of WASP-156 from Sectors 4, 31, 42 and 43 (top panel, orange dots) – note the breaks on the time axis. Subtracting the fitted red noise (middle panel) from the observations yields the blue dots of the top panel. The best fit transit model is shown with continuous red line. The residuals are plotted on the bottom panel.

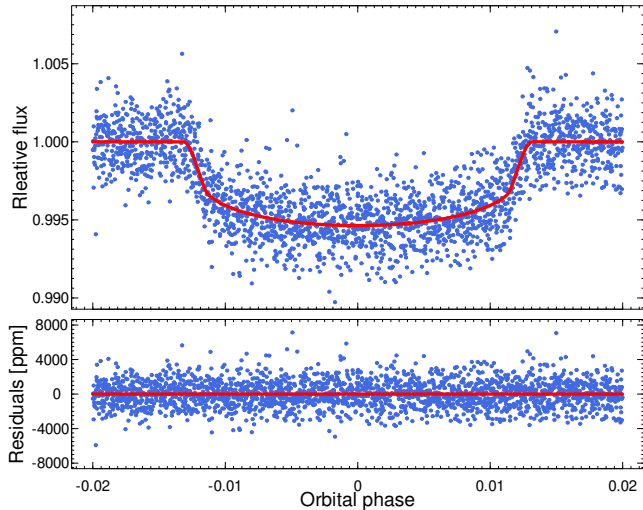


Figure 8. Phase-folded TESS light curve of WASP-156 without correlated noise (top panel, blue dots), the best fit transit model (top panel, solid red line) and the residuals (bottom panel).

are shown on the upper panels of Figs. 9, 10 and 11. The residuals (bottom panels of Figs. 9, 10 and 11) indicate that most of the time-correlated noise was removed by the wavelet-formulation incorporated into TLCM.

The quadratic limb-darkening coefficients were computed with PyLDTk for the three filters and were fixed during the fitting process. The uncertainty in the limb-darkening coefficients was taken into account by fitting u_+ and u_- with the inclusion of a Gaussian prior with a central value set according to the theoretical values listed in Table 2 and width of 0.05 in every case. The other parameters, P , t_C , a/R_S , R_P/R_S , σ_r and σ_w were set as free parameters of the fit. As we solve the light curves in the same way for every case, including the TESS and PLATO data, we have a homogeneous way of uncertainty estimation, which allows for a better comparison between different filters/instruments. We also note that all uncertainties derived during our analyses correspond to the 1σ level. Beside the transit parameters from individual filters, the combined values for each parameter was estimated as the weighted mean of the value from the three individual fits, while the combined uncertainty is equal to one-third of the square root of the sum of the individual uncertainties.

4.1.1 LTT 9779 b with Ariel

The transit parameters of LTT 9779 from the simulated Ariel observations (Fig. 9) are shown in Table 7. The t_C values are all consistent with 0, meaning that the correlated noise was removed thoroughly enough for it not to be able to mimic transit timing variations. All other parameters are within 1σ of the input values, with the exception of $R_P/R_{S,FGS2}$ at 1.3σ . Fig. 15 shows the wavelength-(in)dependence of the fitted planetary radii. The fitted σ_w , representing the point-to-point scatter of the white noise in

Table 7. Derived transit parameters for LTT-9779 b, TOI-674 b and WASP-156 b from the three filters of Ariel and the combined values.

Parameter	VISPhot	FGS1	FGS2	Combined
<i>LTT 9779 b</i>				
a/R_S	3.772 ± 0.041	3.782 ± 0.040	3.790 ± 0.044	3.784 ± 0.024
R_P/R_S	0.04569 ± 0.00101	0.04519 ± 0.00075	0.04493 ± 0.00064	0.04533 ± 0.00047
b	0.9223 ± 0.0040	0.9215 ± 0.0032	0.9231 ± 0.0030	0.9223 ± 0.0020
P [days]	0.792065 ± 0.000016	0.792067 ± 0.000011	0.792060 ± 0.000009	0.792064 ± 0.000007
t_C [days]	0.000104 ± 0.00034	-0.000064 ± 0.000237	0.000027 ± 0.000185	0.000032 ± 0.000150
u_+	0.81 ± 0.06	0.64 ± 0.05	0.51 ± 0.06	–
u_-	0.66 ± 0.07	0.43 ± 0.07	0.29 ± 0.07	–
σ_r [100 ppm]	294.202 ± 4.058	243.431 ± 2.885	159.460 ± 2.714	–
σ_w [100 ppm]	3.854 ± 0.017	2.897 ± 0.014	2.924 ± 0.013	–
<i>TOI-674 b</i>				
a/R_S	11.73 ± 0.28	12.10 ± 0.16	11.87 ± 0.11	11.93 ± 0.11
R_P/R_S	0.11220 ± 0.00139	0.11209 ± 0.00058	0.11227 ± 0.00033	0.11223 ± 0.00051
b	0.693 ± 0.021	0.672 ± 0.013	0.686 ± 0.008	0.683 ± 0.009
P [days]	1.977150 ± 0.000029	1.977175 ± 0.000011	1.977170 ± 0.000007	1.977171 ± 0.000011
t_C [days]	0.000194 ± 0.000270	0.000007 ± 0.000096	-0.000038 ± 0.000062	-0.000017 ± 0.000097
u_{1+}	0.76 ± 0.06	0.61 ± 0.04	0.43 ± 0.03	–
u_{1-}	0.32 ± 0.07	0.13 ± 0.06	0.02 ± 0.07	–
σ_r [100 ppm]	913.641 ± 35.007	425.538 ± 10.116	304.506 ± 5.217	–
σ_w [100 ppm]	21.297 ± 0.097	7.873 ± 0.035	4.626 ± 0.021	–
<i>WASP-156 b</i>				
a/R_S	12.91 ± 0.20	12.92 ± 0.28	12.78 ± 0.29	12.88 ± 0.15
R_P/R_S	0.06637 ± 0.00060	0.06729 ± 0.00057	0.06689 ± 0.00050	0.06687 ± 0.00032
b	0.112 ± 0.104	0.173 ± 0.121	0.198 ± 0.127	0.155 ± 0.068
P [days]	3.836167 ± 0.000085	3.836304 ± 0.000052	3.836159 ± 0.000048	3.836218 ± 0.000037
t_C [days]	-0.000346 ± 0.000350	-0.000651 ± 0.000214	0.000121 ± 0.000204	-0.000261 ± 0.000154
u_{1+}	0.80 ± 0.05	0.61 ± 0.04	0.53 ± 0.03	–
u_{1-}	0.76 ± 0.06	0.41 ± 0.06	0.29 ± 0.06	–
σ_r [100 ppm]	22.217 ± 25.088	249.831 ± 6.241	251.481 ± 5.159	–
σ_w [100 ppm]	12.994 ± 0.034	7.445 ± 0.019	6.302 ± 0.017	–

the light curves, are lower in all three filters (at 50, 37 and 38 ppm \sqrt{h}) compared to the input values. This apparent discrepancy arises because of two factors: (i) the wavelet-based noise filter does not remove all autocorrelated effects from the light curve; it reduces them, and (ii) the simple white noise models generated here actually pseudo-random by nature, thus they may include some autocorrelated effects.

The inner precision of the combination of Ariel filters during the simulated 30-day observation is higher than what can be computed from the two sectors of TESS measurements, with the exception of P , the uncertainty of which should improve with a longer time series. Most notably, the planet-to-star radius ratio is with a $\sim 1\%$ precision, which is crucial for estimates of the bulk composition of this planet.

4.1.2 TOI-674 b with Ariel

Simulating one-minute cadence light curves in the three filters of Ariel for TOI-674 b (Fig. 10) yields the transit parameters shown in Table 7. The fitted transit midtimes are consistent with 0 in every pass-band. In the case of VISPhot and FGS1, all fitted transit parameters are within 1.3σ and 1σ of their input values, respectively. In FGS2, the retrieved relative planetary radius is higher by 2σ , the semi-major axis is lower by 2.5σ , and the impact parameter is

also higher higher by 2σ . These discrepancies are below the 3σ threshold for statistical significance, however, they also influence the combined values of the transit parameters, yielding values that are within 2σ of their respective values derived from the TESS light curves. The fitted planetary radii are plotted as a function of wavelength in Fig. 16.

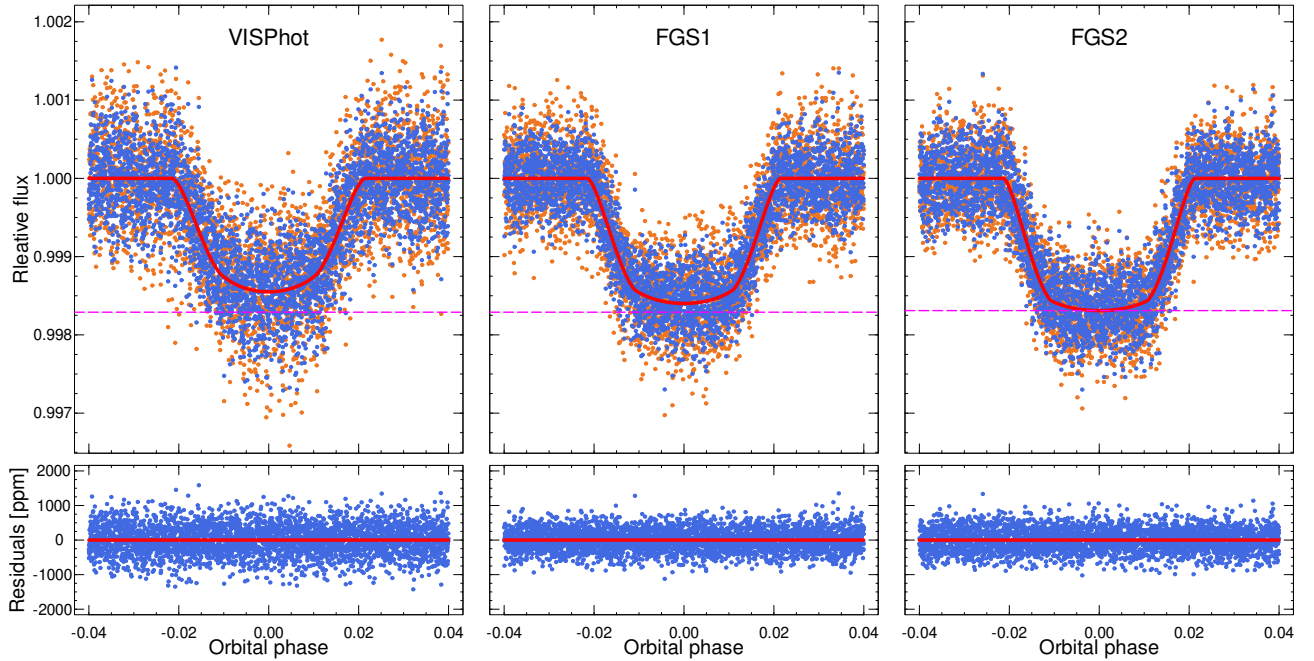
Because of the light curves are solved by TLMC in every case, we may also say that the thirty-day-long simulated Ariel observations can improved the precision of the transit parameters in comparison to the three sectors of TESS (with the exception of P). Most notably, the R_P/R_S has an relative uncertainty of 0.45% from the combination of the three filters. Furthermore, the fitting process yielded the following estimates for the white noise levels: 274, 102 and 59 ppm \sqrt{h} in VISPhot, FGS1 and FGS2, respectively. As in the case of LTT 9779, these noise levels are lower in comparison with the standard deviation of the input noise models (Table 1).

4.1.3 WASP-156 b with Ariel

The resulting transit parameters from the three narrow-band filters of Ariel (Fig. 11) are shown in Table 7. Similarly to the case of LTT 9779 b, the t_C values are consistent with zero in VISPhot and FGS2. All of the fitted transit parameters are within 1.3σ from their respective input values in VISPhot and FGS2. In FGS1, the

Table 8. Transit parameters of the giraffes from the two considered cases of possible observations: using all four camera groups or using just one.

Parameter	LTT 9779 b	TOI-674 b	WASP-156 b
<i>24 cameras</i>			
a/R_S	3.786 ± 0.038	12.00 ± 0.34	12.75 ± 0.34
R_P/R_S	0.04564 ± 0.00050	0.11435 ± 0.00103	0.06584 ± 0.00071
b	0.9233 ± 0.0025	0.682 ± 0.025	0.21 ± 0.14
P [days]	0.7920650 ± 0.0000047	1.977156 ± 0.000027	3.836109 ± 0.000046
t_C [days]	0.000006 ± 0.000097	0.000035 ± 0.000200	3.83627 ± 0.00019
u_+	0.64 ± 0.04	0.63 ± 0.05	0.76 ± 0.03
u_-	0.38 ± 0.07	0.00 ± 0.07	0.56 ± 0.06
σ_r [100 ppm]	111.154 ± 1.426	293.602 ± 9.936	210.455 ± 3.796
σ_w [100 ppm]	2.108 ± 0.006	22.834 ± 0.067	5.549 ± 0.016
<i>6 cameras</i>			
a/R_S	3.795 ± 0.045	11.92 ± 0.34	12.27 ± 0.53
R_P/R_S	0.04553 ± 0.00072	0.11486 ± 0.00139	0.06783 ± 0.00094
b	0.9228 ± 0.0030	0.685 ± 0.025	0.35 ± 0.12
P [days]	0.7920378 ± 0.0000084	1.977131 ± 0.000046	3.836087 ± 0.000076
t_C [days]	0.00056 ± 0.00018	0.00024 ± 0.00039	3.83632 ± 0.00032
u_+	0.65 ± 0.06	0.67 ± 0.06	0.63 ± 0.04
u_-	0.38 ± 0.07	0.10 ± 0.08	0.49 ± 0.06
σ_r [100 ppm]	89.840 ± 2.587	178.388 ± 19.262	236.760 ± 5.087
σ_w [100 ppm]	4.231 ± 0.012	44.872 ± 0.131	10.919 ± 0.027

**Figure 9.** Simulated LTT 9779 b light curves in the three narrow-band filters of Ariel (top panel, orange). Removing the correlated noise yields the blue dots of the top panel. The best-fit transit models are plotted with solid red lines. The residuals are shown in the bottom row. For easier visual differentiation between the different filters, a dashed magenta line is plotted at the minimum of the FGS2 model curve.

time of midtransit shows a non-zero values at 3σ , and the orbital period has a 2.8σ offset from the derived TESS results, biasing in turn the combined results as well. Because Ariel will observe simultaneously in all three bandpasses, such discrepancies can be handled by excluding the data from the filter where the significant offset in t_C is detected, as it can not have astrophysical origins.

The fitted R_P/R_S values for TESS, VISPhot, FGS1 and FGS2 are shown on Fig. 17.

4.2 Transit parameters from PLATO

We have selected two 30-day sections of the simulated PLATO light curves where the drift is the most significant (one where the obser-

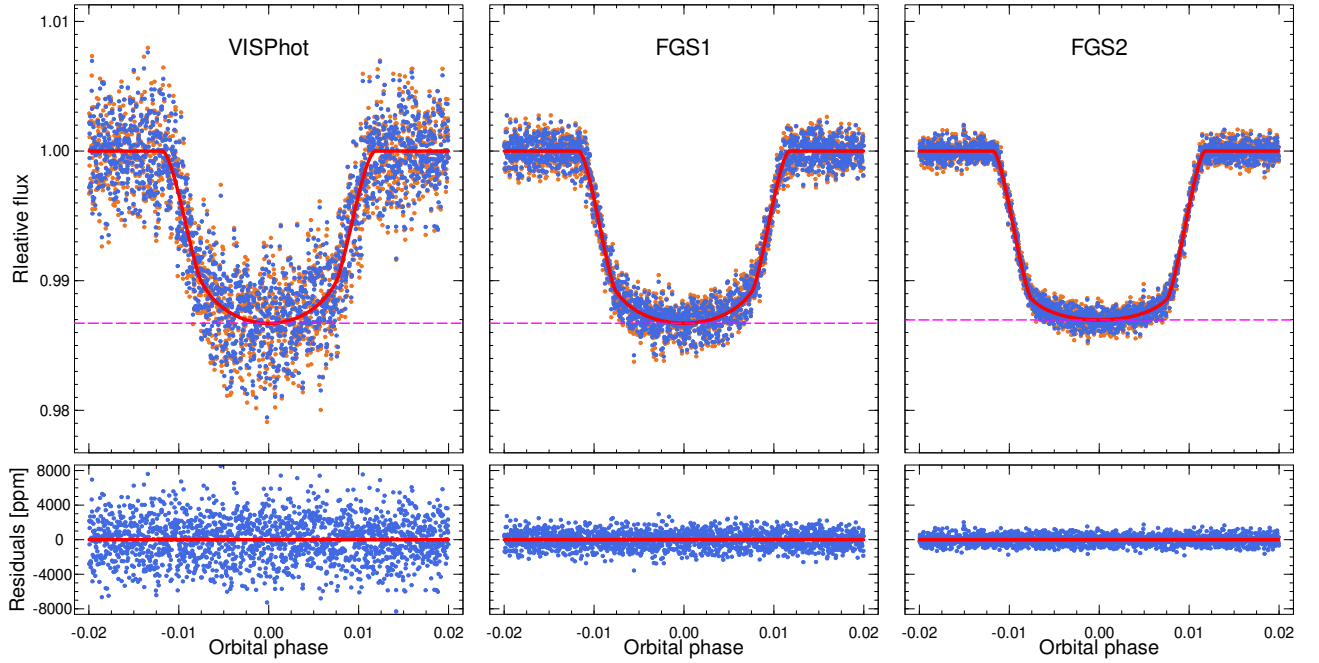


Figure 10. Same as Fig. 9 but for TOI-674.

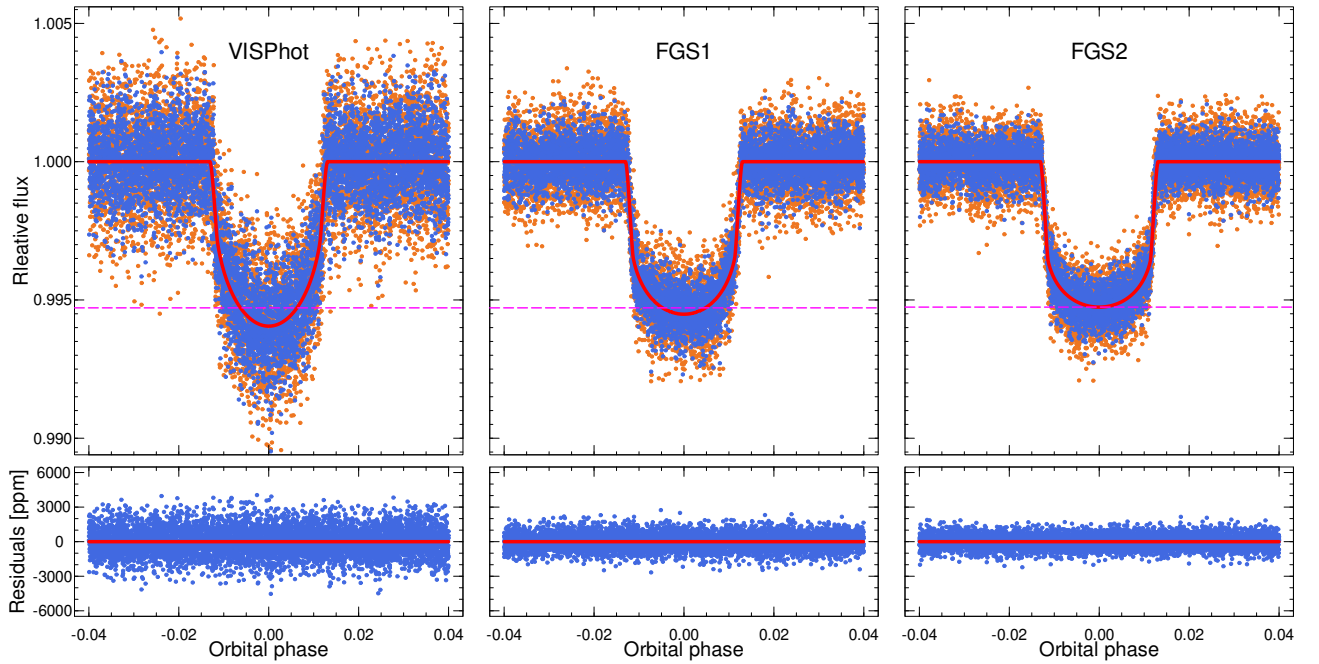


Figure 11. Same as Fig. 9 but for WASP-156.

vations are accomplished with all 24 cameras and one where only 6 cameras are used). This was done in order to have a better comparison to the *Ariel* simulations and to reduce the computational time. The simulated light curves (for the 24-camera case) are shown on the top panels Figs. 12, 13 and 14, the best-fit transit parameters are shown on the top and middle panels of these figures, while the residuals are plotted on the bottom panels. Similarly to the analysis of the *Ariel* data, the limb darkening coefficients were fitted by ap-

plying a Gaussian prior with a mean set to the theoretical values of Table 2 and a width of 0.05.

4.2.1 *LTT 9779 b* with *PLATO*

The light curve from the 24-camera-observations of *LTT 9779 b* is plotted in Fig. 12; the transit parameters from the two considered cases are shown in Table 8. The two resulting parameter sets are

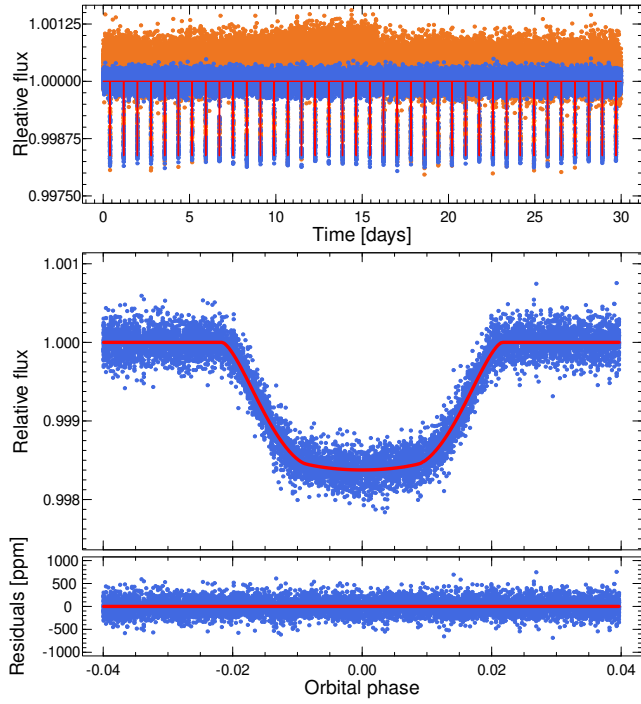


Figure 12. Simulated LTT 9779 observations with 24 cameras of PLATO (top panel, orange), best-fit transit model (top panel – as a function of time and middle panel – as a function of orbital phase) and the light curve with the correlated noise removed (blue dots). The residuals are shown on the bottom panel. For plotting purposes, only every other point is shown.

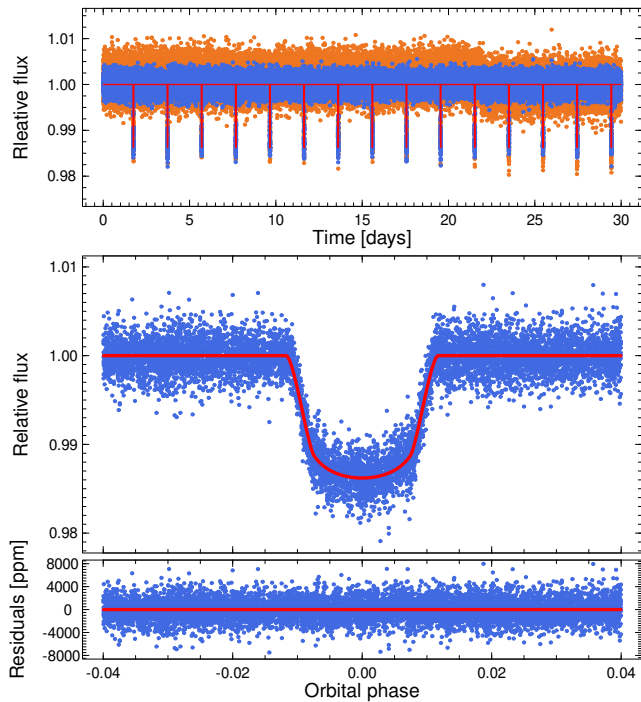


Figure 13. Same as Fig. 12 but for TOI-674.

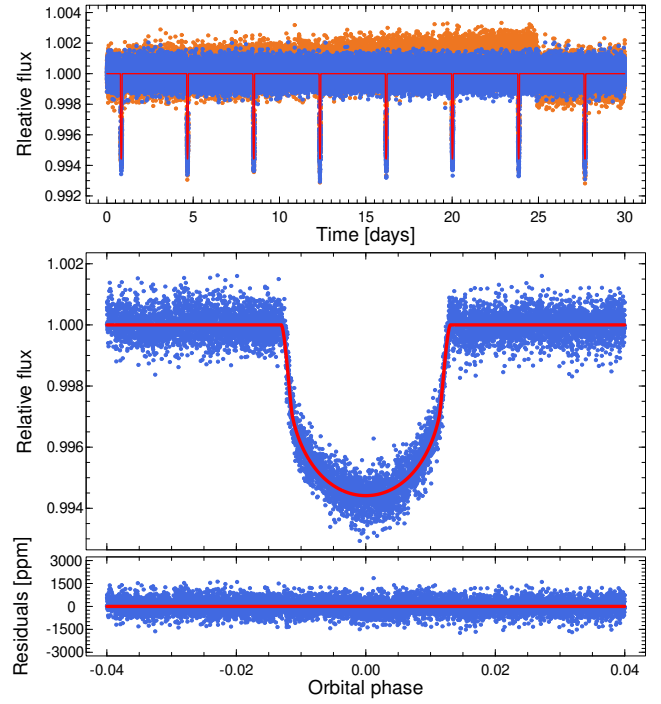


Figure 14. Same as Fig. 12 but for WASP-156.

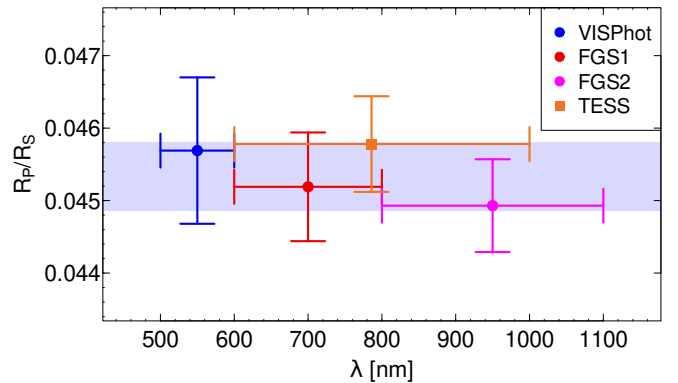


Figure 15. Comparison of the planetary radii fitted in the three bandpasses of Ariel (blue, red, and magenta) and TESS (orange) for LTT 9779 b. The shaded blue area represents the combination of the three photometric filters.

consistent with each other and are within 1σ from the input data (obtained from the TESS light curves) for a/R_S , R_P/R_S and b . When we consider the 6-camera-case, the higher noise levels (Table 1) induce a 3σ discrepancy between the input and fitted parameters, while t_C is also not compatible with 0 (t_C and P are known to be correlated).

Based on σ_w , the white noise levels of 18 and 35 ppm \sqrt{h} are slightly lower than shown in Table 1. The planet-to-star radius ratio can be retrieved with a relative precision of 1.1% and 1.6%.

4.2.2 TOI-674 b with PLATO

Simulated PLATO observations of TOI-674 using all four camera groups are plotted in Fig. 13. The retrieved transits are deeper than the input, represented by the R_P/R_S values that are higher by 2.6 σ

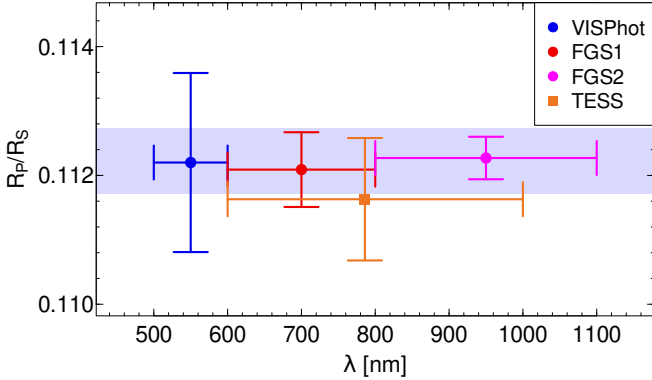


Figure 16. Same as Fig. 15 but for TOI-674 b.

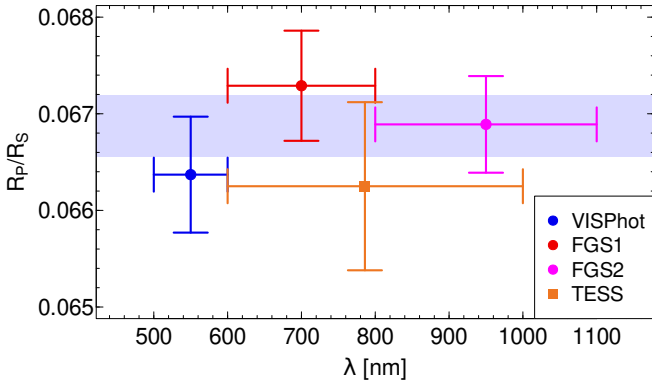


Figure 17. Same as Fig. 15 but for WASP-156 b.

and 2.3σ in comparison to the TESS data, for the 24 and 6 camera cases, respectively. All other retrieved parameters agree within the estimated uncertainties with their input values. The fitted time of midtransit is also consistent with 0 in both cases. The nominal precision for the star-to-planet radius ratio is 0.9% and 1.2% for the two considered cases of observations. The fitted σ_w values, representing the detected white noise in the system, corresponding to 183 and 374 ppm \sqrt{h} for the two considered cases. These values are slightly lower than the level of noise that is superimposed onto the simulated light curves (Table 1).

4.2.3 WASP-156 b with PLATO

The simulated observations of WASP-156 with PLATO using the more favorable case where the target is observed by all 24 cameras as well as the best-fit models are plotted in Fig. 14. In both considered scenarios, the fitted transit parameters (Table 8) are within 1.6σ of the input values (derived from analyzing the TESS light curve). They are also consistent with each other as well as the *Ariel* simulations. The estimated time of midtransit is consistent with 0. Similarly to the simulated *Ariel* light curves, the white noise parameter is slightly lower than the standard deviation of the noise on the light curves at 46 and 91 ppm \sqrt{h} .

One key benefit of the simulations with both upcoming telescopes is that they will present considerable improvements in the precision of the known transit parameters, especially in comparison to the current TESS measurements. In the case of WASP-156

b, we can retrieve R_p/R_s with a nominal precision of 1.1% and 1.4% from the 30-day simulated PLATO observations with the two considered scenarios.

5 DISCUSSION

The significance of the presented simulations relies on the ability of the giraffe planets being test-beds for those scenarios of planet formation and evolution which are related to atmospheric mass-loss. The observational evidence point to a multiple structure behind the sub-Jovian desert/savanna (Szabó et al. 2023). Since its boundaries were proven to be marked by different planets, very probably reflecting different processes, one being more effective in the period–mass parameter spaces, and the other one in the period–radius parameter space. In Szabó et al. (2023) I, we also discussed that the majority of observations support the irradiation-driven loss of the atmosphere (Owen & Murray-Clay 2018; Szabó & Kálmán 2019), and the other scenario can likely be the high-eccentricity migration (Owen & Lai 2018).

We suggest that the significance of the irradiation-driven loss of atmosphere can be directly studied in the case of those planets which are presumably on their way outwards the savanna, and we can reliably assume that they are currently suffering the processes that make the savanna mostly empty. The giraffe planets, being in a location of the parameter space which is otherwise empty, are this kind of test targets. More precisely, there are two scenarios that can retain the giraffe planets inside the savanna: they can either be (1) planets that have recently got into their current position, and due to the processes that empty the savanna, these planets are evolving towards the boundaries within a short time scale, or (2) these are stable positions of these planets, which can be reside inside the savanna for a long time because some specific property protects them from the processes that depose all other planets.

Concerning possibility (2), although planets (or stripped planetary cores) that are dense enough might survive in the savanna such as TOI-849 b (Armstrong et al. 2020), there have been no single parameter or simple combination of parameters found as of now that are certain to protect the planets inside the savanna, while the time scale of photoevaporation of close-in planets can be as short as one million years (Lecavelier Des Etangs 2007), and hence the explanation (1) seems to be more likely to us. Also, according to dos Santos et al. (2021), the boundary of the savanna is populated by several exoplanets with significant atmospheric escape (dos Santos et al. 2021, and references therein). However, in either of these cases, the precise determination of planet parameters can reveal the reasons behind the formation of the savanna itself – either by observing how planets *leave* the savanna, or by observing how they can *survive*.

The photoevaporation of planets is a process which was observed in the case of a few exoplanets, and it’s detection –if it really is reshaping the giraffe planets– is promising. A feature of photoevaporation is a metallicity-dependent thermal cooling (Demangeon et al. 2018b; Petigura et al. 2018), which can be revealed by a highly sensitive thermal analysis of the atmosphere (although the effect is superimposed on a complicated thermal map which itself can have prominent asymmetries (e.g. Knutson et al. 2007; Agol et al. 2010; Lendl et al. 2020). Such observations could be made by analyzing the phase curves and eclipses of the planets, which is more easily done in infra-red due to the temperatures expected on the planet (see e.g. Agol et al. 2010; Cowan & Fujii 2018) in combination with spectroscopic observations which can be used to probe the

atmosphere directly. This is therefore clearly a task well-suited for Ariel.

Another, and quite routinely observed feature linked to irradiation-driven loss of atmosphere is the presence of tenuous gas envelopes around the exoplanets. These features can be detected in the transmission spectra taken during the transits in either atomic lines (e.g. [Nortmann et al. 2018](#)) or molecules (e.g. [Macintosh et al. 2015](#)), the latter of which will be possible with the Ariel InfraRed Spectrometer (see [Changeat et al. \(2020\)](#) for details). A photometric feature related to the atmospheric envelope is the wavelength-dependent transit depth, caused by the molecular bands in the IR spectrum, and the wavelength-dependence of the total scattering cross section of a planet with a chemical gradient in an extended upper atmosphere/ionosphere (e.g. [Edwards et al. 2020](#)), with a spectacular example being the detection of CO₂ in the atmosphere of WASP-39 b using JWST ([The JWST Transiting Exoplanet Community Early Release Science Team et al. 2022](#)). In the case of TOI-674 b, [Murgas et al. \(2021\)](#) attempted to constrain the wavelength-dependent transit depth based on Spitzer and HST measurements and found evidence of water vapor, a feature that could be observed by Ariel with higher significance.

A third observation can be the time-dependence of R_p , due to the loss of material and the destruction of an overinflated atmosphere, which can appear with a transit light curve atmosphere in the case of material loss with a comet-like intensity ([Rappaport et al. 2012](#); [Garai 2018](#)). Variability in the transit depth and shape may occur on timescales as short as weeks–months as in the case of K2-22 b ([Sanchis-Ojeda et al. 2015](#)). As both wavelength and time-dependence of R_p can be expected, a baseline planetary radius is necessary which can not be reliably determined from observations at a singular passband, or from IR spectrophotometry. Our proposed observing scenario can therefore only be carried out via Ariel, whereas the chief purpose of PLATO observations would be monitoring the time-dependence.

In case of future JWST observations (a facility that would of course be capable of completing a similar, though not identical, program) of these specific targets, follow-up Ariel observations would be even more crucial for a simultaneous search for time and wavelength-dependence. However, contrary to JWST, the primary focus of Ariel will be observations of exoplanetary systems. Given that the key for higher precision would be observations of many transits and not the size of the primary mirror, Ariel is more suitable for such a program.

Observations with the IR spectrograph of Ariel would also add a great deal of new information to the presented ideas. To complete such simulations, introduction of many unknown atmospheric parameters would be mandatory. The best exploitation of spectrophotometry with Ariel will be explored in [Szabó et al \(in prep\)](#).

These observations have a very promising future prospects in the forthcoming years. The discovery of new giraffe planets can be expected from PLATO ([Rauer et al. 2014](#)), reaching a fainter detection limit than TESS ([Ricker et al. 2015](#)). Due to the short orbital period of these planets, an observation time covering approximately one TESS Sector (≈ 28 days with gaps) will be enough for a secure detection (and this is why we expect TESS already have discovered most of the giraffe planets within its observable sky). The observational history of transit depths of exoplanets in optical bands, including but not limited to the Kepler ([Borucki et al. 2010](#)), TESS, CHEOPS ([Benz et al. 2021](#)), and being expected from PLATO and Ariel ([Tinetti et al. 2021](#)) will cover 2 decades for many exoplanets, leading to precise radii. Transmission spec-

tra with the James Webb Space Telescope will be also a standard tool for atmospheric studies in exoplanet (e.g. [Rustamkulov et al. 2022](#)). Also, time evolution of R_p/R_s or asymmetries in the transit light curve can reveal atmospheric evaporation or disintegration (although currently known transit depth variations are linked to nodal precession instead (e.g. [Szabó et al. 2012, 2020](#)), chromospheric activity ([Miller-Ricci et al. 2008](#); [Agol et al. 2010](#)) or inhomogeneities of the stellar surface ([Szabó et al. 2022c](#))).

There are also several other systems which are argued to be in the sub-Jovian savanna (including NGTS-4 b, NGTS-10 b, TOI-2196 etc.), and as we argued in [Szabó et al. \(2023\)](#), the savanna itself has no firm border and has a multitude of planets near it. It is also reasonable to expect that there are other unknown or uncharacterized (a task suited for PLATO) such planetary systems. Therefore even if these specific targets are not observed by Ariel, direct observational evidence for the appearance of the savanna can be gained from measurements of many other candidates similar to the giraffes explored in this paper. This paper should be regarded as a proof of concept instead of a direct definition of a specific study.

6 SUMMARY AND CONCLUSION

The area in the $R_p - P$ and $M_p - P$ parameter spaces formerly known as the sub-Jovian/Neptune desert ([Szabó & Kálmán 2019](#)) is by now known to be not entirely empty ([Jenkins et al. 2020](#); [Murgas et al. 2021](#)) hence we proposed its conversion into the “sub-Jovian savanna”. In this paper, we selected three known exoplanets that are either in the sub-Jovian savanna (such as LTT 9779 b and TOI-674 b), or are on its border (such as WASP-156 b) to explore how future the two future ESA missions (PLATO and Ariel) might help resolve the complex processes behind the formation of the savanna (see [Owen & Lai \(2018\)](#) and [Szabó et al. \(2023\)](#) for details).

As the selected objects inhabit the “savanna”, we also coined the term giraffe planets. First we analysed all available TESS data of these giraffes (two, three, and four Sectors for LTT 9779, TOI-674 and WASP-156, respectively) with TLCDM. In general, our transit parameters are in good agreement with the previously published results of [Jenkins et al. \(2020\)](#); [Saha & Sengupta \(2021\)](#); [Murgas et al. \(2021\)](#). Our analysis of the TESS light curves improved the precision of these parameters, which is the result of the inclusion of more data and the wavelet-based noise handling of TLCDM.

We used the transit parameters derived from the TESS analysis as input to the simulated Ariel and PLATO observations. In the case of Ariel, we devised an algorithm to simulate the most realistic observations using the three narrow passbands (VISPhoT, FGS1 and FGS2). The transits (simulated with the *batman* software package) were injected into a time series consisting of white noise (based on ArielRad calculations) and red noise (based on Kepler light curves of stars similar to the hosts) which included both stellar and instrumental noise sources. In the case of the simulated PLATO observations, we made use of PLS to create PLATO-like noise that does not include any astrophysical effects and injected the transits into it. As the PLATO fields are not yet fixed, we have no knowledge of how these targets might be observed or if they will be observed at all. We therefore considered the most and least favorable cases (observations with all 24 cameras and with just six camera). It is also reasonable to expect that in case these exact targets are not observed at all, other giraffe planets should be discovered before the launch of PLATO and during its operation.

The simulated light curves were solved with TLCDM. In the case of the three Ariel filters, the light curves were solved independently

and the parameters were then combined, yielding constraints on the star-to-planet ratio with precision $\sim 1\%$. In the case of PLATO, the selected 30-day-long light curves resulted in transit parameters estimated with higher precision than the currently available TESS data, in both considered cases. The estimated uncertainties for the PLATO simulations were slightly higher than the results of the combined *Ariel* observations. We elected not to include astrophysical noise sources in the PLATO simulations for the following reasons. (i) by adding more noise, the uncertainties of the transit would be at least as large as the ones estimated in Table 8, which are already less precise than the *Ariel* data. (ii) a direct comparison between the light curves obtained from the three different telescopes will not be possible for the any real observations due to the different approaches for observations of each facility. If PLATO were to observe these specific targets, we would have light curves spanning at least 90 days (Nascimbeni et al. 2022), which would ultimately yield higher precision than these simulations. (iii) allocating time for any targets will be more challenging with *Ariel*, as it will observe ≈ 1000 targets (Tinetti et al. 2021), also, the simultaneous photometric and spectroscopic measurements will only be possible by *Ariel*, thus a more thorough analysis of the feasibility of these observations is warranted. (iv) if there will be observations of PLATO of these targets, those would serve as extraordinary follow-up measurements to the pre-existing TESS data, regardless of the actual precision of the transit parameters.

The giraffe planets can be golden targets for the *Ariel* mission, because the simultaneous photometry and spectroscopy enables the comparison of the transit depth in the visual and infrared bands, which is a possibility to immediately recognise atmospheric processes related to loss of atmosphere. The measurements can be repeated, and the dynamics or possible variations in evaporation rates will be also revealed. In atmospheric studies, the planet radius is an important input parameter which appears in several mutual parameter degenerations. The most sensitive detection of the atmospheric loss requires an accurate, prior information about the planet radius, while the radius itself is degenerated with stellar limb-darkening coefficients as well (Csizmadia et al. 2013). As the disintegration of these planets can be expected, changes in the transit shape would introduce further degeneracies between the transit parameters. *Ariel* will be capable of a simultaneous observation of the transit light curve in 3 optical bands and break up the degeneracy between the planet radius and the limb-darkening. This will lead to an unbiased and precise radius determination (Szabó et al. 2022b) and together with the simultaneously taken transmission spectra in the infrared (Tinetti et al. 2021), the structure of the upper atmosphere will be revealed. We suggest that the homogeneous studies of the giraffe planets with *Ariel* should be a key study in the formation and evolution of close-in planets.

DATA AVAILABILITY

The simulated *Ariel* and PLATO light curves are available in Open Science Framework, at https://osf.io/vyrx9/?view_only=a2bf4b774f884ac4866af2c1436393d9.

ACKNOWLEDGEMENTS

The authors thank M. Bergemann and G. Morello for their valuable comments. This work was supported by the PRODEX Experiment Agreement No. 4000137122 between the ELTE Eötvös

Loránd University and the European Space Agency (ESA-D/SCI-LE-2021-0025). Support of the Lendület LP2018-7/2021 grant of the Hungarian Academy of Science, and the KKP-137523 ‘SeismoLab’ Élvonal grant as well as the grant K-138962 of the Hungarian Research, Development and Innovation Office (NKFIH) are acknowledged. LBo acknowledges the funding support from Italian Space Agency (ASI) regulated by “Accordo ASI-INAf n. 2013-016-R.0 del 9 luglio 2013 e integrazione del 9 luglio 2015”. Project no. C1746651 has been implemented with the support provided by the Ministry of Culture and Innovation of Hungary from the National Research, Development and Innovation Fund, financed under the NVKDP-2021 funding scheme.

This work presents results from the European Space Agency (ESA) space mission PLATO. The PLATO payload, the PLATO Ground Segment and PLATO data processing are joint developments of ESA and the PLATO Mission Consortium (PMC). Funding for the PMC is provided at national levels, in particular by countries participating in the PLATO Multilateral Agreement (Austria, Belgium, Czech Republic, Denmark, France, Germany, Italy, Netherlands, Portugal, Spain, Sweden, Switzerland, Norway, and United Kingdom) and institutions from Brazil. Members of the PLATO Consortium can be found at <https://platomission.com/>. The ESA PLATO mission website is <https://www.cosmos.esa.int/plato>. We thank the teams working for PLATO for all their work

REFERENCES

- Agol E., Cowan N. B., Knutson H. A., Deming D., Steffen J. H., Henry G. W., Charbonneau D., 2010, *ApJ*, **721**, 1861
- Armstrong D. J., et al., 2020, *Nature*, **583**, 39
- Benz W., et al., 2021, *Experimental Astronomy*, **51**, 109
- Borucki W. J., et al., 2010, *Science*, **327**, 977
- Brandt J., et al., 2022, arXiv e-prints, p. arXiv:2201.04197
- Carter J. A., Winn J. N., 2009, *ApJ*, **704**, 51
- Changeat Q., Al-Refaie A., Mugnai L. V., Edwards B., Waldmann I. P., Pascale E., Tinetti G., 2020, *AJ*, **160**, 80
- Claret A., 2000, *A&A*, **363**, 1081
- Cowan N. B., Fujii Y., 2018, in Deeg H. J., Belmonte J. A., eds., *Handbook of Exoplanets*. p. 147, doi:10.1007/978-3-319-55333-7_147
- Crossfield I. J. M., et al., 2020, *ApJ*, **903**, L7
- Csizmadia S., 2020, *MNRAS*, **496**, 4442
- Csizmadia S., Pasternacki T., Dreyer C., Cabrera J., Erikson A., Rauer H., 2013, *A&A*, **549**, A9
- Csizmadia S., Smith A. M. S., Cabrera J., Klagyivik P., Chaushev A., Lam K. W. F., 2021, arXiv e-prints, p. arXiv:2108.11822
- Demangeon O. D. S., et al., 2018a, *A&A*, **610**, A63
- Demangeon O. D. S., et al., 2018b, *A&A*, **610**, A63
- Dragomir D., et al., 2020, *ApJ*, **903**, L6
- Edwards B., et al., 2020, *AJ*, **160**, 8
- Eigmüller P., et al., 2019, *A&A*, **625**, A142
- Fazio G. G., et al., 2004, *ApJS*, **154**, 10
- Gaia Collaboration et al., 2016, *A&A*, **595**, A2
- Gaia Collaboration et al., 2018, *A&A*, **616**, A1
- Garai Z., 2018, *A&A*, **611**, A63
- Gerber J. M., Magg E., Plez B., Bergemann M., Heiter U., Olander T., Hoppe R., 2022, arXiv e-prints, p. arXiv:2206.00967
- Gustafsson B., Edvardsson B., Eriksson K., Jørgensen U. G., Nordlund Å., Plez B., 2008, *A&A*, **486**, 951
- Heller R., Harre J.-V., Samadi R., 2022, arXiv e-prints, p. arXiv:2206.02071
- Huber D., et al., 2014, *ApJS*, **211**, 2
- Husser T.-O., Wende-von Berg S., Dreizler S., Homeier D., Reiners A., Barman T., Hauschildt P. H., 2013, *A&A*, **553**, A6
- Jenkins J. S., et al., 2020, *Nature Astronomy*, **4**, 1148
- Kálmán S., Szabó M. G., Csizmadia S., 2022a, arXiv e-prints, p. arXiv:2208.01716

- Kálmán S., Bókon A., Derekas A., Szabó G. M., Hegedűs V., Nagy K., 2022b, *A&A*, 660, L2
- Knutson H. A., et al., 2007, *Nature*, 447, 183
- Kreidberg L., 2015, *PASP*, 127, 1161
- Lecavelier Des Etangs A., 2007, *A&A*, 461, 1185
- Lendl M., et al., 2020, *A&A*, 643, A94
- Lightkurve Collaboration et al., 2018, Lightkurve: Kepler and TESS time series analysis in Python, Astrophysics Source Code Library (ascl:1812.013)
- Macintosh B., et al., 2015, *Science*, 350, 64
- Mandel K., Agol E., 2002, *ApJ*, 580, L171
- Mazeh T., Holczer T., Faigler S., 2016, *A&A*, 589, A75
- Miller-Ricci E., et al., 2008, *ApJ*, 682, 593
- Morello G., Claret A., Martin-Lagarde M., Cossou C., Tsiara A., Lagage P.-O., 2020a, *The Journal of Open Source Software*, 5, 1834
- Morello G., Claret A., Martin-Lagarde M., Cossou C., Tsiaras A., Lagage P. O., 2020b, *AJ*, 159, 75
- Mugnai L. V., Pascale E., Edwards B., Papageorgiou A., Sarkar S., 2020, *Experimental Astronomy*, 50, 303
- Murgas F., et al., 2021, *A&A*, 653, A60
- Nascimbeni V., et al., 2022, *A&A*, 658, A31
- Nortmann L., et al., 2018, *Science*, 362, 1388
- Owen J. E., Lai D., 2018, *MNRAS*, 479, 5012
- Owen J. E., Murray-Clay R., 2018, *MNRAS*, 480, 2206
- Parviainen H., Aigrain S., 2015, *MNRAS*, 453, 3821
- Persson C. M., et al., 2022, arXiv e-prints, p. arXiv:2208.05797
- Petigura E. A., et al., 2018, *AJ*, 155, 89
- Rappaport S., et al., 2012, *ApJ*, 752, 1
- Rauer H., et al., 2014, *Experimental Astronomy*, 38, 249
- Ricker G. R., et al., 2015, *Journal of Astronomical Telescopes, Instruments, and Systems*, 1, 014003
- Rustamkulov Z., Sing D. K., Liu R., Wang A., 2022, *ApJ*, 928, L7
- Saha S., Sengupta S., 2021, *AJ*, 162, 221
- Samadi R., et al., 2019, *A&A*, 624, A117
- Sanchis-Ojeda R., et al., 2015, *ApJ*, 812, 112
- Smith A. M. S., et al., 2021, *A&A*, 646, A183
- Szabó G. M., Kálmán S., 2019, *MNRAS*, 485, L116
- Szabó G. M., Kiss L. L., 2011, *ApJ*, 727, L44
- Szabó G. M., Pál A., Derekas A., Simon A. E., Szalai T., Kiss L. L., 2012, *MNRAS*, 421, L122
- Szabó G. M., Pribulla T., Pál A., Bódi A., Kiss L. L., Derekas A., 2020, *MNRAS*, 492, L17
- Szabó G. M., et al., 2022a, *Experimental Astronomy*, 53, 607
- Szabó G. M., et al., 2022b, *Experimental Astronomy*, 53, 607
- Szabó G. M., et al., 2022c, *A&A*, 659, L7
- Szabó G. M., Kálmán S., Borsato L., Hegedűs V., Mészáros S., Szabó R., 2023, *A&A*, 671, A132
- The JWST Transiting Exoplanet Community Early Release Science Team et al., 2022, arXiv e-prints, p. arXiv:2208.11692
- Tinetti G., et al., 2021, arXiv e-prints, p. arXiv:2104.04824
- West R. G., et al., 2019, *MNRAS*, 486, 5094
- Wheatley P. J., et al., 2018, *MNRAS*, 475, 4476
- Yang F., Chary R.-R., Liu J.-F., 2022, *AJ*, 163, 42
- dos Santos L. A., et al., 2021, *A&A*, 649, A40

This paper has been typeset from a $\text{\TeX}/\text{\LaTeX}$ file prepared by the author.